Low-Power and ppm-Level Multimolecule Detection by Integration of Self-Heated Metal Nanosheet Sensors

Takahisa Tanaka, Kenta Tabuchi, Kohei Tatehora, Yohsuke Shiiki, Shuya Nakagawa,
Tsunaki Takahashi, *Member, IEEE*, Ryota Shimizu, Hiroki Ishikuro, *Member, IEEE*,
Tadahiro Kuroda, *Fellow, IEEE*, Takeshi Yanagida, and Ken Uchida, *Member, IEEE*

Abstract—H_2 and NH_3 detection with low power consumption was demonstrated by integrated chemiresistive Pt and PtRh nanosheet sensors on glass substrates. The self-heating effects realized low power and local heating of metal nanosheet sensors, enabling the integration of sensors with different operating temperatures. Based on different resistance changes in Pt and PtRh nanosheets toward H_2 and NH_3, the concentration of each gas was detected from a gas mixture by consuming around 1-mW power. For decreasing the power consumption and further integration of sensors, sensor scaling and pulsed operations were numerically and experimentally studied. In addition to good connectivity of metal nanosheet sensors to large-scale integration (LSI) circuits, improvements of the power consumption by sensor scaling were proven. The pulsed operations required for integrated sensor arrays maintained a sensor response, or a resistance change, of approximately 60%, even when the power consumption was reduced by 20%.

Index Terms—Gas sensors, nanosheet, self-heating, sensor arrays.

I. INTRODUCTION

IN THE Internet of things (IoT) era, gas sensors play an important role in edge devices. Small gas sensors consuming low power can detect explosives for security and serve as biomarkers for breath analysis in healthcare applications. In practical application, gas sensors should detect target gases from gas mixtures comprising several types of chemical species. Gas sensor arrays consisting of different sensors have been used for target gas detections in gas mixtures [1]–[5]. However, densely integrated gas sensor arrays operating with low power consumption are not sufficiently developed.

Chemiregistors, or typical gas sensors, are suitable for integration due to simple two-terminal structures of sensing parts. On the other hand, most of the chemiresistors such as metal–oxide semiconductors operate at high temperature [6]–[8]. Thermal energy is required for acceleration of chemical reactions which generate sensor responses, and optimum operating temperatures depend on target gases and sensor materials. Generally, external heaters supply the thermal energy [2]–[4], [6]–[8]. The external heaters unnecessarily heat the surroundings, thereby causing additional power consumption. Furthermore, the heated surroundings disturb the integration of gas sensors with different optimum operating temperatures. In some works, the self-heating effects of gas sensors have been used to locally rise temperatures [9]–[11]. The power consumption of the self-heated sensors can be reduced by reducing the sizes of the sensors. However, the power consumptions of the reported sensors in previous studies were in the order of several mW to W, and the integration of the sensors was not achieved.

Therefore, in this work, self-heated metal nanosheet sensors were integrated. A sufficiently high temperature was locally realized with an input power of approximately 1 mW. Catalytically active Pt and PtRh nanosheets were used for gas detection. Operating both metal nanosheets at optimum operating temperatures, ppm-level H_2 and NH_3 were successfully detected, based on the different catalytic activities of the metal nanosheets. For further suppression of power consumption and integration of the metal nanosheet sensors, scaling of sensor sizes and pulsed operations were experimentally and numerically studied. Experimental comparisons of sensor responses during continuous and pulsed operations revealed that the pulsed operations reduce the power consumption while maintaining the sensor response. Although preliminary results were reported in [12], this article describes the experiments and analysis in greater detail for understanding the thermal properties of metal nanosheet sensors as thermal equivalent circuits; estimations of the operating temperatures of self-heated metal nanosheet sensors and the temperature dependence of sensor responses are discussed. Furthermore, toward practical application, sensor responses were measured during long-time self-heating operation. These newly added explanations and results help understand the experimental procedures and clarify the temperature characteristics and the durability of metal nanosheet sensors during self-heating.
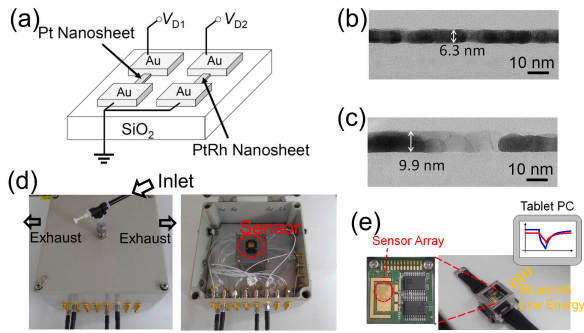
Fig. 1. (a) Schematic of the metal nanosheet sensor array. Cross-sectional TEM images of (b) Pt and (c) PtRh nanosheets. (d) Photographs of (left) outside and (right) inside of the measurement system. (e) Photographs of the wristwatch-type sensing system. This system is based on the results obtained from a project commissioned by NEDO.
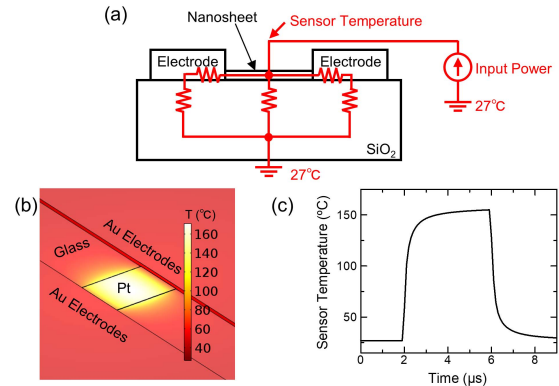

Fig. 2. (a) Schematic cross section of the sensor and superimposed thermal equivalent circuit at steady-state. (b) Numerically simulated temperature profile around the self-heated metal nanosheet sensor at a steady-state. The L/W ratio of the metal nanosheet was 2.0 μm/1.5 μm. The input power was 1.1 mW. (c) Time dependence of the temperature at the center of the metal nanosheet. Electric power of 1.1 mW was input from 2 to 6 μs.

II. EXPERIMENTAL

The schematic of the metal nanosheet sensor array is shown in Fig. 1(a). The metal nanosheet channels were formed by patterning through either maskless photolithography or electron-beam (EB) lithography followed by EB deposition on the glass substrates. The channel length/width (L/W) ratios of the photolithography-patterned metal nanosheet sensors were 2.0 μm/1.5 μm and 2.0 μm/1.8 μm, respectively. The thickness of the Pt and the PtRh nanosheets were approximately 6 and 10 nm, respectively. To investigate the effects of narrowing the channels, the channel length/width ratio of the EB-lithography-patterned metal nanosheet sensors was 2.0 μm/0.1 μm. After the fabrication of each metal channel, 30 min of annealing at 400 °C in N_2 atmosphere was performed for improving adhesion. Cross-sectional transmission electron microscopy (TEM) images of the Pt and the PtRh nanosheets are shown in Fig. 1(b) and (c), respectively. Polycrystalline metal nanosheets are observed. Fig. 1(d) illustrates the experimental setup. Gas sensing was carried out by blowing gas at a flow rate of 500 mL/min to the metal nanosheet sensors. The concentration of the sprayed gas was controlled by mass flow controllers to contain H_2 and NH_3 in the range of 0–100 ppm and 0–5 ppm, respectively. To analyze the sensor performance, the time dependence of the electric current of the metal nanosheet sensors was measured by the Keithley 2636A sourcemeter with applying constant bias voltage. The responses of the metal nanosheet sensors were defined by the resistance changes normalized by the initial resistances. As shown in Fig. 1(e), to demonstrate low power operation in a practical system, gas sensing by the metal nanosheet sensor array on the wristwatch-type system was also performed. This sensing system was driven by a Li-ion polymer battery without any external wired connections. The sensor resistances measured by a bridge circuit were wirelessly transferred to a personal computer through Bluetooth low energy.

III. SENSING MECHANISM

The Pt and PtRh nanosheets sensed H_2 and NH_3 based on the changes in their resistances resulting from catalytic reactions on their surfaces [13]–[15]. As discussed in [16] for

H_2 sensing by Pt nanowires, surface electron scatterings induced by adsorbates change the resistance of the metal nanosheets. As the density of states induced by the adsorbates near the Fermi energy decreases, surface electron scatterings become more specular from diffusive [17]. From density functional calculations in [18], the density of states induced by oxygen atoms on the Pt surface is greater than the density of states induced by hydrogen atoms. Therefore, catalytically generated hydrogen atoms reduce the resistance of the Pt nanosheets. The sensing mechanism of the PtRh nanosheets was assumed to be the same as that of the Pt nanosheets because of their similar composition.

The selectivity of our metal nanosheet sensors would be equal to the selectivity of catalytic reactions on Pt. Previous works reported selective H_2 detection by thermoelectric H_2 sensors which detect thermal energy induced by catalytic reactions of the Pt-loaded ceramics [19], [20]. Due to the similarity of the origin of the sensing mechanism, our sensors are expected to have enough selectivity to typical interference volatile organic compounds such as CO, CH_4, i-C_4H_{10}, C_2H_5OH, and CH_3OH.

To accelerate the catalytic reactions, the temperatures of the metal nanosheet sensors were controlled by the self-heating effects. Under steady-states, the temperatures can be estimated from the powers supplied to the metal nanosheet sensors and a thermal equivalent circuit as shown in Fig. 2(a). The temperature at the bottom of the glass substrates was assumed to be 27 °C. Joule heating mainly occurred in the metal nanosheets because the resistances of the metal nanosheets were sufficiently greater than those of the electrodes. The low thermal conductivities of the glass substrates caused large temperature rises in the metal nanosheets with the small input powers. The temperature rises were numerically simulated by COMSOL Multiphysics software, as shown in Fig. 2(b). Using the temperature at the center of the metal nanosheets, a thermal resistance of 1.28×10^5 °C/W was derived. Fig. 2(c) shows the time dependence of the temperature of the metal nanosheet. As the heat capacities of the metal nanosheets were small,
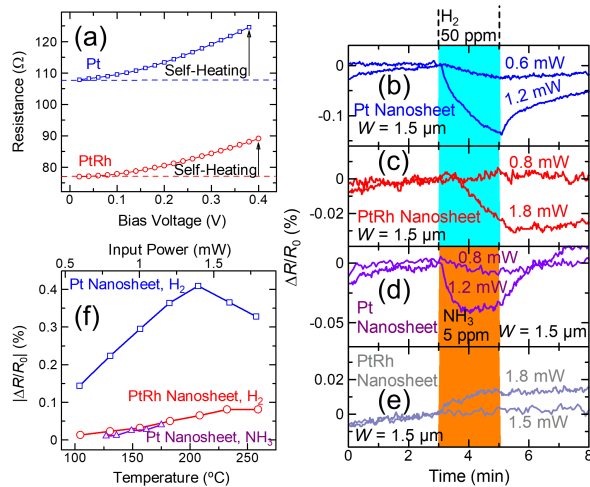
Fig. 3. (a) Bias voltage dependence of the resistances of the Pt and the PtRh nanosheets. Time-dependent sensor responses of (b) Pt and (c) PtRh nanosheets to H_2. Time-dependent sensor responses of (d) Pt and (e) PtRh nanosheets to NH_3. (f) Temperature dependence of the sensor responses of the nanosheet sensors. H_2 and NH_3 concentrations were 100 and 5 ppm, respectively. The sensor temperature shown as the bottom axis was estimated from the input power and the numerically obtained thermal resistance of $1.28 \times 10^5 °C/W$.

temperature changes within a microsecond order were possible. In our pulsed operations, voltage changes were sufficiently slow, and the metal nanosheet sensors were in steady-states. Therefore, the temperatures in the metal nanosheet sensors could be estimated from the thermal resistance.

IV. RESULTS AND DISCUSSION

Fig. 3(a) shows the resistance–voltage characteristics for the Pt and the PtRh nanosheet sensors. The temperature rise by the self-heating effects was confirmed from the increase in the resistance with the increase in the bias voltage. Fig. 3(b) and (c) shows the sensor response of the Pt and the PtRh nanosheet sensors to H_2, respectively. By the increase in the input power, a clear sensor response to H_2 was observed. Fig. 3(d) and (e) shows the sensor response of the Pt and the PtRh nanosheet sensors to NH_3, respectively. Similar to the H_2 sensing, the sensor response to NH_3 was observed by the Pt nanosheet sensor. On the other hand, the sensor response to NH_3 was hardly observed by the PtRh nanosheet sensor. At the input power of 1.8 mW, the resistance of the PtRh nanosheet sensor was slightly increased by NH_3. This increase in the resistance was observed only when the NH_3 concentration was 5 ppm or higher. The mechanism of the resistance increase is not clear. However, insensitiveness or resistance increase in the PtRh nanosheets to NH_3 is useful for gas recognition by the Pt and the PtRh nanosheet sensors.

For the Pt and the PtRh nanosheet sensors, the absolute values of the resistance changes to target gases were small. However, the noise levels were also small, and the signal-to-noise ratios were high. For the sensor responses to 50 ppm H_2, the signal-to-noise ratios of the Pt the PtRh nanosheet sensors were 85 and 12, respectively. Therefore, by appropriate signal amplification, we can extract the sensor signals in practical usage.
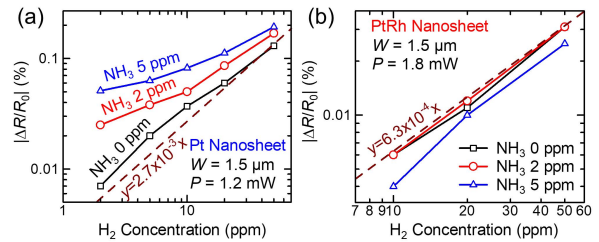

Fig. 4. Sensor responses of (a) Pt and (b) PtRh nanosheets to gas mixtures in terms of H_2 concentration. Exposure time to the gas mixtures is 2 min. The dashed lines were linear approximations of H_2 concentration dependences of sensor responses. The initial resistance R_0 of Pt and PtRh is 125 and 89 Ω, respectively.

The high input power requirement of the PtRh nanosheet sensors means that the PtRh nanosheet sensors require a high temperature. Fig. 3(f) shows the temperature dependence of the responses of the Pt and the PtRh nanosheet sensors. The sensor temperatures were estimated from the thermal resistance and the input powers. According to Fig. 3(f), the temperature at which the response to H_2 is maximized is lower for the Pt nanosheet sensor than for the PtRh nanosheet sensor. The temperature dependence of the sensor responses is governed by the catalytic reactions and the adsorption/desorption at the sensor surfaces. At low temperature, the sensor responses increase with increasing temperatures because of acceleration of the catalytic reactions. On the other hand, at high temperature, the adsorption of target gases is inhibited and the desorption of adsorbates is promoted, resulting in decreased sensor responses. Optimum operating temperature at which sensor response is maximized depends on sensor materials and target gases. Therefore, local temperature controls by the self-heating effects are important for integrations of gas sensors.

Fig. 4(a) and (b) shows the sensor responses to gas mixtures in terms of the H_2 concentration. The Pt and the PtRh nanosheet sensors were operated around their optimal operating temperatures. For gas sensing of a single target gas in several minutes, the sensor responses are proportional to the gas concentration. Thus, although there are individual differences in response value of each sensor, calibration of the sensors is possible by measuring a single target gas of a known concentration.

From the H_2 concentration dependence of the sensor responses in Fig. 4(a) and (b), similar selectivities as in Fig. 3(b)–(e) were observed. The response of the Pt nanosheet sensor increased not only for H_2 but also for NH_3. On the other hand, the PtRh nanosheet sensor mainly responded to H_2. Based on the difference in their selectivities to H_2 and NH_3, the concentration of each gas in gas mixtures could be determined separately. Fig. 5(a) shows the results of eight measurements at five gas concentrations using the sensor array. Fig. 5(b) shows the results of the principal component analysis of the sensor responses in Fig. 5(a). Among the sensor responses measured by the same sensor, the reproducibility was high. Therefore, the data points for each gas concentration are clearly separated, and the first and the second principal components depend on the H_2 and NH_3 concentrations, respectively.
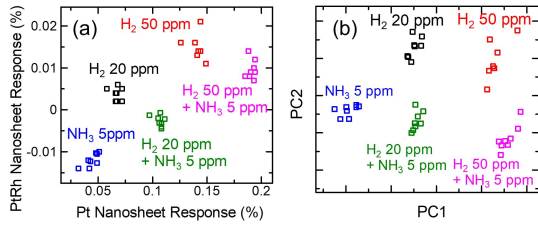
Fig. 5. (a) 2-D plot showing sensor responses of Pt ($R_0 = 124\ \Omega$ and input power = 1.2 mW) and PtRh ($R_0 = 89\ \Omega$ and input power = 1.8 mW) nanosheets to gas mixtures with H_2 and NH_3. Exposure time to the gas mixtures is 2 min. (b) Results of principle component analysis of sensor responses given in (a).
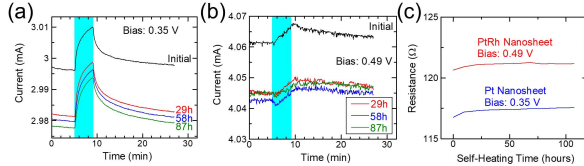

Fig. 6. Sensor response of (a) Pt and (b) PtRh nanosheets during continuous self-heating. Exposed gas contained 100 ppm H_2. (c) Resistance of Pt and PtRh nanosheets during continuous self-heating for over 100 h. Measured Pt and PtRh nanosheets were different from nanosheets measured in Figs. 3(a)–(f), 4(a) and (b), and 5(a) and (b).
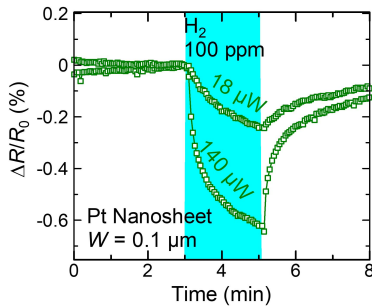

Fig. 7. Response to H_2 obtained using the EB-lithography-patterned Pt nanosheet sensor. The initial sensor resistance $R_0 = 1.26$ kΩ.

Fig. 8. Benchmark of H_2 sensors. The sensor size is defined excluding the electrode area. Specs of recently reported thermoelectric [5], Pd nanowire [11], ReRAM [23], FET [24], Pellistor [25], and MEMS [26] sensors are also shown.

TABLE I
BENCHMARKS OF SENSOR RESPONSES TO H_2

Sensor Material, Strucrure	Limit of Detection	Reference
Pt, Nanosheet	2 ppm	This Work
PtRh, Nanosheet	10 ppm	This Work
Pt/Al$_2$O$_3$, Thermoelectric	0.5 ppm[a]	[27]
Pd, Nanowire	5 ppm	[11]
Pt/Al$_2$O$_3$, Pellistor	200 ppm	[25]
Pd$_{78}$Cu$_5$Si$_{17}$, MEMS	500 ppm	[26]
Pt/Ta$_2$O$_5$, ReRAM	1000 ppm	[23]
Pt, FET	1000 ppm	[24]

work [22], the change in cross-sectional shapes from nanosheets to nanowires was expected to increase the sensor responses by up to three times because the surface contributing to electron scattering was changed from one top plane to one top plane and two side planes. Therefore, scaling of the metal nanosheet sensors reduces the power consumptions and improves the scale of integrations and the sensor responses. The benchmarks of our sensors and the recently reported H_2 sensors [5], [11], [23]–[26] are shown in Fig. 8. We can see that our sensor shows excellent performance in terms of both the sensor size and the power consumption. In Table I, we also compare the detection limit of our sensors with those of the reported sensors plotted in Fig. 8 [11], [23]–[27]. Although the detection limit of our sensors was not the best among those of previously reported sensors, our sensors are enough sensitive for performing breath analysis [28] and detecting leakage of H_2 whose explosion limit is 4%.

The metal nanosheet sensors require glass substrates to realize high temperatures at the sensors, while large-scale integration (LSI) circuits are on the Si substrates. For evaluating the performance of large-scale integrated metal nanosheet sensors with the LSI circuits, sensor arrays on a glass substrate with through-glass vias (TGVs) [29], [30] were considered, as shown in Fig. 9(a). The metal nanosheet sensors were placed between two adjacent vias. The parameters for the numerical simulation are listed in Table II. Based on these assumed parameters, 1250 sensors can be integrated per square millimeter. As there are approximately 200–300 types of chemical substances in human exhaled breath [31], it is considered that breath sensing will be possible if metal nanosheet sensors with different selectivities are integrated with the structure as shown in Fig. 9(a).

The self-heated sensors are with large current density at high temperature. However, the current densities and the temperatures of our sensors were lower than a typical electro-migration condition [21]. To confirm the durability of the metal nanosheet sensors, H_2 sensings and resistance measurements were performed during long self-heating operation over 100 h as shown in Fig. 6(a)–(c). Although the sensor resistances differed between the first 20 h and beyond, gradual resistance changes by the self-heating operation did not cause serious effects on H_2 sensings.

Although the power consumptions of the sensors patterned through maskless photolithography were in the mW order, the power consumption can be further decreased by reducing the sensor size. Fig. 7 shows the response of the sensor patterned by EB lithography. The self-heating activated sensor response was observed even at the input power in the sub-mW level. Based on the numerically simulated thermal resistance of $5.2 \times 10^5\,°$C/W, the sensor temperatures of 100 °C and 36 °C at input powers of 140 and 18 μW were estimated, respectively. For the sensors patterned by EB lithography, the aspect ratio defined by width/thickness was approximately 16. Further reduction in the width of the sensors will improve the sensor responses. According to the previous theoretical
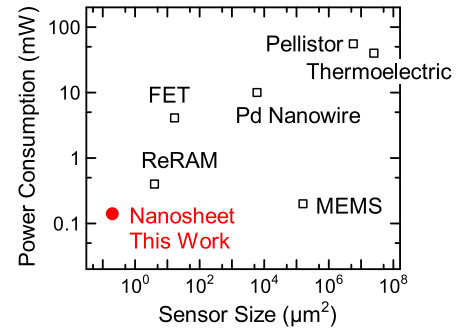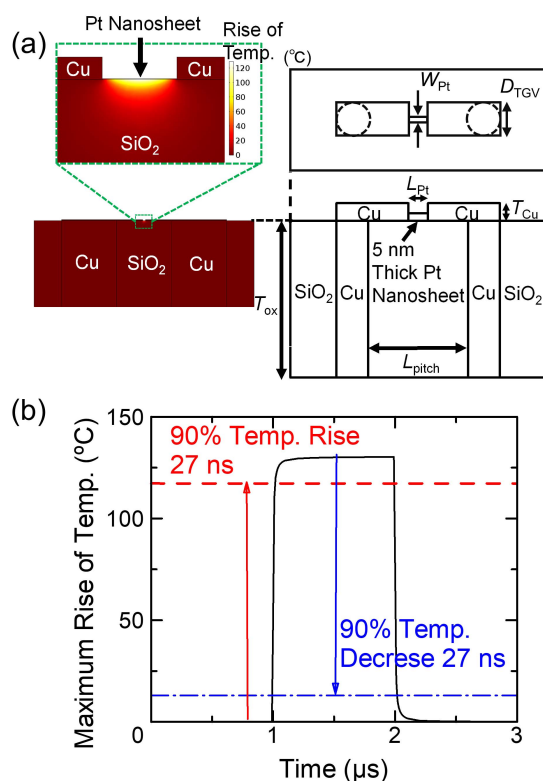
Fig. 9. (a) Numerically simulated metal nanosheet with TGV structure. (b) Time dependence of sensor temperature. Power was applied between 1 and 2 μs.

TABLE II
SIMULATION PARAMETERS FOR SENSOR WITH TGVs

Simulation Parameters			
Input Power	0.15 mW	D_{TGV}	10 μm
T_{Pt}	5 nm	L_{Pitch}	10 μm
L_{Pt}	500 nm	T_{OX}	100 μm
W_{Pt}	50 nm	T_{Cu}	150 nm

Although the self-heating effects become difficult owing to the high thermal conductivity of the TGVs, the sensor temperature of approximately 120 °C is generated at the input power of 0.15 mW as shown in Fig. 9(a). If the integrated metal nanosheet sensors are operated continuously, the sensor array consumes power in the sub-W range per square millimeter. Therefore, pulsed operations are required for practical usage of large-scale integrated sensor arrays. The metal nanosheet sensors with TGV structures could change the sensor temperature faster than the metal nanosheet sensors fabricated in the experiments, as shown in Fig. 9(b). By alternately operating the metal nanosheet sensors with pulsed operations, large-scale integrated sensor arrays can be operated with realistic power consumption.

The catalytic reactions were accelerated at high temperature. In pulsed operations, a decrease in the duty ratio decreases the time when the sensor temperature is high. This implies that the pulsed operations reduce the sensor responses. Fig. 10 shows the comparison of the experimental sensor responses derived from continuous and pulsed operations. For the pulsed operation, rectangular pulse with a frequency of 2 Hz and
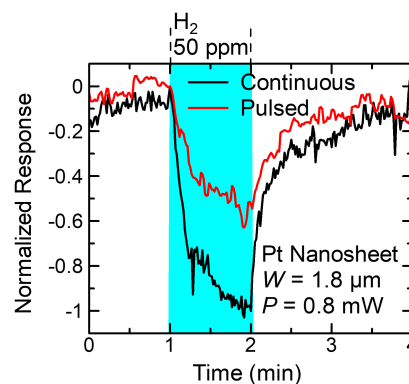

Fig. 10. Responses of the Pt nanosheet sensor derived from the continuous operation and the pulsed operations.
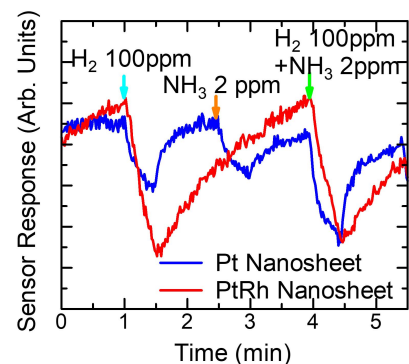

Fig. 11. Wirelessly transferred sensing data of Pt and PtRh nanosheet sensors.

a duty ratio of 0.2 was used. As the duty ratio is 0.2, the sensor responses during the pulsed operation are expected to be 20% of those during the continuous operation. However, the experimentally observed sensor response during the pulsed operation was 60% of that during the continuous operation.

The high sensitivity during the pulsed operation is caused by a two-step reaction on the sensor surface. For H_2 sensing, the H_2 molecules are first physically adsorbed on the sensor surface. The adsorbed H_2 molecules are then chemically decomposed by the catalytic reactions. The molecular impingement rate is inversely proportional to the square root of the temperature. On the other hand, the rate of the catalytic reactions increases exponentially with temperature. Therefore, the physical adsorption of molecules is promoted at low temperature, and the chemical catalytic reaction is promoted at high temperature. The continuous operations of the metal nanosheet sensors suppress either the physical adsorption or the chemical catalytic reaction. On the other hand, in the pulsed operations, a low-temperature surface is formed in the OFF states, and a high-temperature surface is formed in the ON states. It was considered that the enhancement in the sensor response was generated by improved physical adsorption of the molecules on the low-temperature surface [32]. Therefore, the pulsed operations have the advantages of both low power operation and maintenance of the sensor responses of the highly integrated sensor array.

To demonstrate low-power and multimolecule detection by pulsed operation of an integrated sensor array on a practical

system, the Pt and the PtRh nanosheet sensors were operated on the wristwatch-type sensing system as shown in Fig. 1(e). The pulse duty ratio is 0.2 and the frequency is 2 Hz. The input powers at the ON states of the pulse are approximately 1.2 and 1.8 mW for the Pt and the PtRh nanosheet sensors, respectively. The Pt and the PtRh nanosheet sensors were operated alternately by shifting the pulse ON state of each sensor. The sensed and wirelessly transferred data are shown in Fig. 11. On the practical system with low power consumption, it was successfully demonstrated that the Pt nanosheet sensor reacted only with H_2 and NH_3, while the PtRh nanosheet sensor reacted only with H_2.

V. CONCLUSION

The Pt and the PtRh nanosheet sensors were integrated on glass substrates. Using the self-heating effects of these metal nanosheets, the sensor responses induced by the catalytic reactions were enhanced. Based on the different selectivities of the Pt and the PtRh nanosheet sensors, the concentrations of H_2 and NH_3 in gas mixtures were successfully categorized. Reduction in power consumption by scaling the sensor channels was experimentally demonstrated, and good connectivity of the metal nanosheet sensor arrays and the LSI circuits was numerically proved. Furthermore, it was possible to decrease power consumption while maintaining sensor response through pulsed operations.

REFERENCES

[1] H. Sundgren, I. Lundström, F. Winquist, I. Lukkari, R. Carlsson, and S. Wold, "Evaluation of a multiple gas mixture with a simple MOSFET gas sensor array and pattern recognition," *Sens. Actuators B, Chem.*, vol. 2, pp. 115–123, May 1990. doi: 10.1016/0925-4005(90)80020-Z.

[2] D.-S. Lee, Y. T. Kim, J.-S. Huh, and D.-D. Lee, "Fabrication and characteristics of SnO2 gas sensor array for volatile organic compounds recognition," *Thin Solid Films*, vol. 416, nos. 1–2, pp. 271–278, Sep. 2002. doi: 10.1016/S0040-6090(02)00619-3.

[3] H.-K. Hong, C. H. Kwon, S.-R. Kim, D. H. Yun, K. Lee, and Y. K. Sung, "Portable electronic nose system with gas sensor array and artificial neural network," *Sens. Actuators B, Chem.*, vol. 66, pp. 49–52, Jul. 2000. doi: 10.1016/S0925-4005(99)00460-8.

[4] A. K. Srivastava, "Detection of volatile organic compounds (VOCs) using SnO2 gas-sensor array and artificial neural network," *Sens. Actuators B, Chem.*, vol. 96, pp. 24–37, Nov. 2003. doi: 10.1016/S0925-4005(03)00477-5.

[5] W. Shin et al., "Thermoelectric array sensors with selective combustion catalysts for breath gas monitoring," *Sensors*, vol. 18, no. 5, p. 1579, May 2018. doi: 10.3390/s18051579.

[6] T. Seiyama, A. Kato, K. Fujiishi, and M. Nagatani, "A new detector for gaseous components using semiconductive thin films," *Anal. Chem.*, vol. 34, no. 11, pp. 1502–1503, Oct. 1962. doi: 10.1021/ac60191a001.

[7] E. Comini, G. Faglia, G. Sberveglieri, Z. Pan, and Z. L. Wang, "Stable and highly sensitive gas sensors based on semiconducting oxide nanobelts," *Appl. Phys. Lett.*, vol. 81, no. 10, pp. 1869–1871, Sep. 2002. doi: 10.1063/1.1504867.

[8] N. Yamazoe, G. Sakai, and K. Shimanoe, "Oxide semiconductor gas sensors," *Catalysis Surv. Asia*, vol. 7, no. 1, pp. 63–75, Apr. 2003. doi: 10.1023/A:1023436725457.

[9] T. Yokoyama, T. Tanaka, Y. Shimokawa, R. Yamachi, Y. Saito, and K. Uchida, "Pd-functionalized, suspended graphene nanosheet for fast, low-energy multimolecular sensors," *ACS Appl. Nano Mater.*, vol. 1, no. 8, pp. 3886–3894, Jul. 2018. doi: 10.1021/acsanm.8b00667.

[10] Y. H. Kim et al., "Self-activated transparent all-graphene gas sensor with endurance to humidity and mechanical bending," *ACS Nano*, vol. 9, no. 10, pp. 10453–10460, Aug. 2015. doi: 10.1021/acsnano.5b04680.

[11] F. Yang, D. K. Taggart, and R. M. Penner, "Joule heating a palladium nanowire sensor for accelerated response and recovery to hydrogen gas," *Small*, vol. 6, no. 13, pp. 1422–1429, Jul. 2010. doi: 10.1002/smll.201000145.

[12] T. Tanaka et al., "Low-power and ppm-level detection of gas molecules by integrated metal nanosheets," in *VLSI Technol. Dig.*, 2019, pp. T158–T159.

[13] A. Spetz, M. Armgarth, and I. Lundström, "Hydrogen and ammonia response of metal-silicon dioxide-silicon structures with thin platinum gates," *J. Appl. Phys.*, vol. 64, no. 3, pp. 1274–1283, Mar. 1988. doi: 10.1063/1.341846.

[14] B. Hellsing, B. Kasemo, and V. P. Zhdanov, "Kinetics of the hydrogen-oxygen reaction on platinum," *J. Catal.*, vol. 132, no. 1, pp. 210–228, Nov. 1991. doi: 10.1016/0021-9517(91)90258-6.

[15] D. G. Löffler and L. D. Schmidt, "Kinetics of NH3 decomposition on polycrystalline Pt," *J. Catal.*, vol. 41, no. 3, pp. 440–454, Mar. 1976. doi: 10.1016/0021-9517(76)90245-1.

[16] F. Yang, K. C. Donavan, S. C. Kung, and R. M. Penner, "The surface scattering-based detection of hydrogen in air using a platinum nanowire," *Nano Lett.*, vol. 12, no. 6, pp. 2924–2930, Apr. 2012. doi: 10.1021/nl300602m.

[17] R. G. Tobin, "Mechanisms of adsorbate-induced surface resistivity— Experimental and theoretical developments," *Surf. Sci.*, vols. 502–503, pp. 374–387, Apr. 2002. doi: 10.1016/S0039-6028(01)01978-1.

[18] T. Tanaka, S. Hoshino, T. Takahashi, and K. Uchida, "Nanoscale Pt thin film sensor for accurate detection of ppm level hydrogen in air at high humidity," *Sens. Actuators B, Chem.*, vol. 258, pp. 913–919, Apr. 2018. doi: 10.1016/j.snb.2017.11.115.

[19] W. Shin, M. Matsumiya, N. Izu, and N. Murayama, "Hydrogen-selective thermoelectric gas sensor," *Sens. Actuators B, Chem.*, vol. 93, pp. 304–308, Aug. 2003. doi: 10.1016/S0925-4005(03)00225-9.

[20] M. Matsumiya, W. Shin, F. Qiu, N. Izu, I. Matsubara, and N. Murayama, "Poisoning of platinum thin film catalyst by hexamethyldisiloxane (HMDS) for thermoelectric hydrogen gas sensor," *Sens. Actuators B, Chem.*, vol. 96, pp. 516–522, Dec. 2003. doi: 10.1016/S0925-4005(03)00630-0.

[21] R. Rusanov, H. Rank, T. Fuchs, R. Mueller-Fiedler, and O. Kraft, "Reliability characterization of a soot particle sensor in terms of stress- and electromigration in thin-film platinum," *Microsyst. Technol.*, vol. 22, no. 3, pp. 481–493, Mar. 2016. doi: 10.1007/s00542-015-2576-6.

[22] E. H. Sondheimer, "The mean free path of electrons in metals," *Adv. Phys.*, vol. 1, no. 1, pp. 1–42, Jan. 1952. doi: 10.1080/00018735200101151.

[23] Z. Wei et al., "From memory to sensor: Ultralow power and high selectivity hydrogen sensor based on ReRAM technology," *IEEE Trans. Electron Devices*, vol. 65, no. 11, pp. 5189–5193, Nov. 2018. doi: 10.1109/TED.2018.2868081.

[24] Y. Sasago, H. Nakamura, Y. Anzai, T. Moritsuka, T. Odaka, and T. Usagawa, "FET-type hydrogen sensor with short response time and high drift immunity," in *VLSI Technol. Dig.*, 2017, pp. T106–T107. doi: 10.23919/VLSIT.2017.7998213.

[25] E. Lee et al., "Micromachined catalytic combustible hydrogen gas sensor," *Sens. Actuators B, Chem.*, vol. 153, no. 2, pp. 392–397, Apr. 2011. doi: 10.1016/j.snb.2010.11.004.

[26] H. Yamazaki, Y. Hayashi, K. Masunishi, D. Ono, and T. Ikehashi, "High sensitivity MEMS capacitive hydrogen sensor with inverted T-shaped electrode and ring-shaped palladium alloy for fast response and low power consumption," *J. Micromech. Microeng.*, vol. 28, no. 9, May 2018, Art. no. 094001. doi: 10.1088/1361-6439/aac21d.

[27] W. Shin et al., "Micro-thermoelectric devices with ceramic combustors," *Sens. Actuators A, Phys.*, vols. 130–131, pp. 411–418, Aug. 2006. doi: 10.1016/j.sna.2006.01.006.

[28] Y. Urita et al., "Breath hydrogen and methane levels in a patient with volvulus of the sigmoid colon," *J. Breath Res.*, vol. 2, no. 3, Sep. 2008, Art. no. 037025. doi: 10.1088/1752-7155/2/3/037025.

[29] S. Takahashi, K. Horiuchi, K. Tatsukoshi, M. Ono, N. Imajo, and T. Mobely, "Development of Through Glass Via (TGV) formation technology using electrical discharging for 2.5/3D integrated packaging," in *Proc. 63rd Electron. Compon. Technol. Conf.*, 2013, pp. 348–352. doi: 10.1109/ECTC.2013.6575594.

[30] M. Töpper et al., "3-D thin film interposer based on TGV (Through Glass Vias): An alternative to Si-interposer," in *Proc. 60th Electron. Compon. Technol. Conf.*, 2010, pp. 66–73. doi: 10.1109/ECTC.2010.5490887.

[31] W. Filipiak et al., "Dependence of exhaled breath composition on exogenous factors, smoking habits and exposure to air pollutants," *J. Breath Res.*, vol. 6, no. 3, Sep. 2012, Art. no. 036008. doi: 10.1088/1752-7155/6/3/036008.

[32] G. Meng et al., "Nanoscale thermal management of single SnO2 nanowire: Pico-Joule energy consumed molecule sensor," *ACS Sens.*, vol. 1, no. 8, pp. 997–1002, Jul. 2016. doi: 10.1021/acssensors.6b00364.